LETTERS

Three-dimensional structure of the myosin V inhibited state by cryoelectron tomography

Jun Liu[1], Dianne W. Taylor[1], Elena B. Krementsova[2], Kathleen M. Trybus[2] & Kenneth A. Taylor[1]

Unconventional myosin V (myoV) is an actin-based molecular motor that has a key function in organelle and mRNA transport, as well as in membrane trafficking[1]. MyoV was the first member of the myosin superfamily shown to be processive, meaning that a single motor protein can 'walk' hand-over-hand along an actin filament for many steps before detaching[2–4]. Full-length myoV has a low actin-activated MgATPase activity at low [Ca^{2+}], whereas expressed constructs lacking the cargo-binding domain have a high activity regardless of [Ca^{2+}] (refs 5–7). Hydrodynamic data and electron micrographs indicate that the active state is extended, whereas the inactive state is compact[8–10]. Here we show the first three-dimensional structure of the myoV inactive state. Each myoV molecule consists of two heads that contain an amino-terminal motor domain followed by a lever arm that binds six calmodulins. The heads are followed by a coiled-coil dimerization domain (S2) and a carboxy-terminal globular cargo-binding domain. In the inactive structure, bending of myoV at the head–S2 junction places the cargo-binding domain near the motor domain's ATP-binding pocket, indicating that ATPase inhibition might occur through decreased rates of nucleotide exchange. The actin-binding interfaces are unobstructed, and the lever arm is oriented in a position typical of strong actin-binding states. This structure indicates that motor recycling after cargo delivery might occur through transport on actively treadmilling actin filaments rather than by diffusion.

Expressed full-length myoV formed two-dimensional (2D) arrays with a hexagonal unit cell ($a = 653$ Å) and a repeating motif that resembles a six-petalled coneflower (Fig. 1a, b). The 'pistil' of the flower contains the motor and cargo-binding domains, and the 'petals' contain the lever arms and the initial segment of the S2 domain. The arrays were extensive but the coherent domains were small, and the poorly sampled diffraction made spatial averaging unproductive. We therefore used correlation averaging and multivariate statistical analysis (MSA) to determine the molecular structure (Fig. 1b–h). This approach allows individual repeats to be aligned with each other independently and to be grouped with self-similar repeats when structural heterogeneity is present[11]. MSA of the flower and molecular repeats (Fig. 1b) reveals details not easily visible in the original micrographs. The major image features can be accounted for by the two motor domains, their lever arms and the S2 domain. The lever arms show a zigzag structure caused by the different orientations of the calmodulins[12]. Between the lever arms, the S2 domain is clearly visible and asymmetrically placed.

The assignment of the motor domains relative to the lever arms could be done in two ways. The favoured 'outward' arrangement (see below) has the motor domains extending roughly along the line of their lever arms (Fig. 1d); the 'inward' arrangement has the motor domains facing each other (Fig. 1e). With the exception of the initial segment of the S2 domain, the various parts of the rest of the tail are not easily separated.

To establish that the arrays consist of folded conformations with the heads bent backwards towards their S2 domain (as opposed to extended conformations, in which S2 could have come from a petal in the adjacent flower), we used MSA on the extracted molecules but included the neighbouring molecule to the outside (Fig. 1f–h). The three class averages revealed variable placement of the neighbouring molecules (Fig. 1f, g), and one of the classes (Fig. 1h) showed no neighbouring molecule. For this class, the S2 domain is as prominent as in the other classes, establishing that the arrays indeed consist of myoV molecules in the folded conformation.

We used electron tomography for three-dimensional (3D) image computation with higher signal-to-noise averages obtained by MSA of the 3D molecular images. In the raw tomogram (Supplementary movie 1) the arrays were readily identified, and flower and molecular

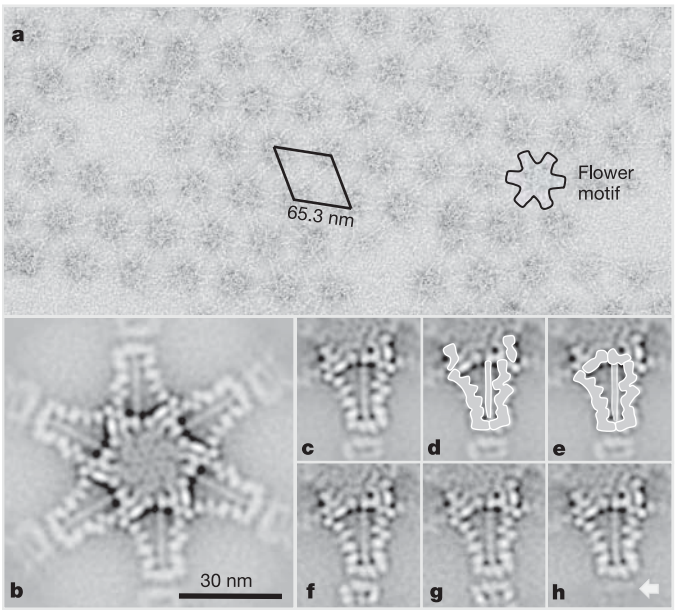

Figure 1 | Electron micrographs and averages of myoV. a, Negatively stained myoV 2D arrays. The 'coneflower' motif is outlined. **b**, Six-fold symmetrized average of 393 myoV coneflower repeats. **c**, Average of 2,358 myoV molecules. **d**, **e**, Two possible interpretations of the projection superimposed on the average: **d** is the outward arrangement and **e** shows the inward arrangement. **f**–**h**, Three different class averages of molecules using a classification mask that included parts of the neighbouring molecule at the bottom. At the bottom the adjacent molecules are different in **f** and **g**, whereas in **h** there is no adjacent molecule (arrow).

[1]The Institute of Molecular Biophysics, Florida State University, Tallahassee, Florida 32306-4380, USA. [2]Department of Molecular Physiology and Biophysics, University of Vermont, Burlington, Vermont 05405-0068, USA.

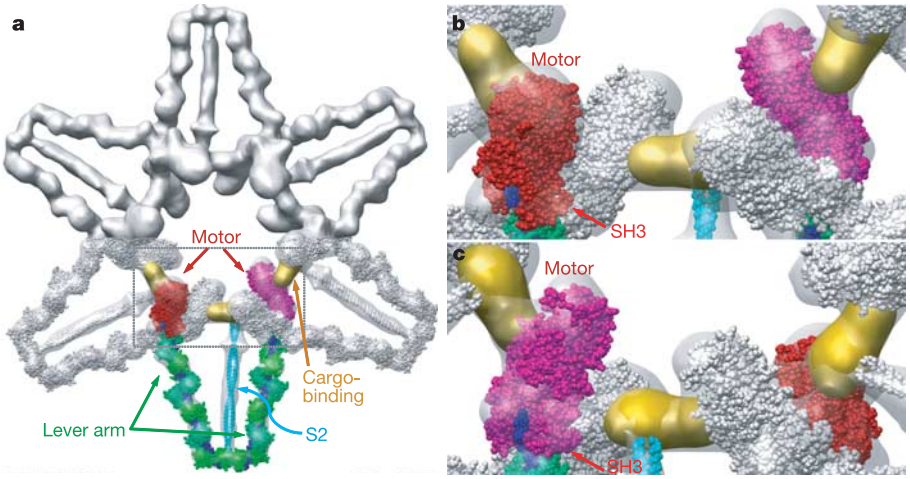

Figure 2 | Molecular arrangement within the 'flower' motif. **a**, At the top is an opaque surface rendering viewed from the solvent phase; at the bottom is a translucent surface view with the myoV atomic model rendered in space filling. The colour scheme for the bottom molecule is as follows: red and magenta, motor domains; green, light chains; blue, heavy chain component of the lever arm; cyan, S2 domain; yellow, cargo-binding domain density envelope; grey, adjacent molecules. **b**, **c**, Higher-magnification views showing the motor domain fit into the density envelope. **b**, View from the solvent phase; **c**, view from the monolayer side.

images could be extracted for alignment and processed as done for the 2D projections. A flower motif generated from the 3D class average with the most molecular images (Fig. 2a, and Supplementary movie 2) shows how six myoV molecules come together. One myoV head lies above (more into the solvent phase than) the head from the adjacent molecule, and their lever arms cross in the vicinity of the first calmodulin.

Array formation has the advantage of reducing conformational variability between individual myoV molecules but has the disadvantage that domain boundaries are sometimes ambiguous. To clarify the molecular boundaries we built an atomic model of the myoV motor domain and lever arm based on two X-ray structures[12,13] (Fig. 2). Two additional models for fitting were built with lever arms in the pre-powerstroke and 90° orientations based on smooth and scallop myosin S1 structures. For calmodulin, the 'closed' conformation[12] was a better fit than the 'open' conformation. Each of the initial models for the myoV heads was tested in both the 'inward' and 'outward' configurations using flexible fitting based on normal mode analysis[14]. The best fit (correlation coefficient of 0.82; Supplementary Methods and slideshow) was obtained for the structure with the post-powerstroke lever-arm orientation in the 'outward' configuration (Figs 1d and 2a).

The rod-like density can account for about 145 residues (about 21 nm) of the S2 domain (Fig. 2a), whereas the initial segment of S2 from sequence analysis consists of about 190 residues (about 28.5 nm)[15]. Some of the S2 sequence must be involved in reversing direction in the inhibited conformation, so the bulge at the end may be the PEST site. The remaining approximately 330 residues before the cargo domain are probably folded up and disordered within the pistil.

An extra density is present between the two motor domains (yellow in Fig. 2) that cannot be accounted for by the atomic model and is presumably the cargo-binding domain. It is positioned on the side opposite the motor domain's actin-binding surface (cyan in Fig. 3) and adjacent to loop 1 (green in Fig. 3). A decrease in the flexibility of loop 1 in myosin II (myoII) has been postulated to decrease ADP release rates[16]. Similarly, direct binding of the cargo-binding domain to loop 1 could stabilize its motion and decrease ADP release rates, thus accounting for the decreased ATPase activity of the folded monomer. The density has a volume corresponding to that predicted for a pair of cargo-binding domains and could be segmented as two separate densities of slightly different sizes. On the basis of the model building, these two closely juxtaposed densities come from different myoV molecules in the lattice. The 15-nm separation of the densities with respect to an individual myoV molecule is within the roughly 20 nm distance observed in electron micrographs of isolated myoV molecules[15].

Although the two myoV heads have different orientations within the arrays (Fig. 2), both have very similar, rigor-like conformations when docked on an actin filament (Fig. 4a, b). Each head can be docked without steric interference from the other head, the S2 domain or the cargo-binding domain. Binding of the inhibited conformation to actin was verified by decorating actin with myoV under conditions used to form the arrays (ADP + P_i). Electron micrographs of negatively stained specimens most commonly revealed extensive decoration (Supplementary Fig. S1). At lower myoV concentration, partial decoration could be achieved. Individual actin-bound molecules showed a triangular shape highly characteristic of our myoV structure (Fig. 4c). The main difference is a less angled lever arm, although this may be an artefact of drying. Our data

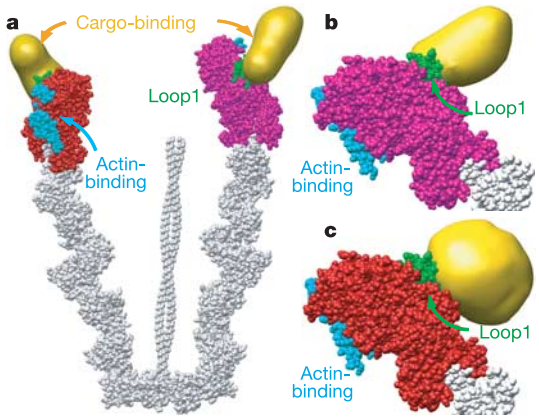

Figure 3 | Placement of the cargo-binding domain on the motor domain. Two cargo-binding domains are resolved that together have a peanut shape. The two motor domains are coloured red and magenta, and their actin-binding surfaces cyan. Loop 1 (residues 184–191) and the ATP-binding region (residues 424–430 and 228–235) are coloured green. The cargo-binding domain is positioned at loop 1. **a**, View from the same direction as Fig. 2a. **b**, Motor domain reoriented to show the relationship between loop 1, the cargo-binding domain and the actin-binding interface. **c**, Same view as **b** for the second motor domain.

therefore indicate that the inhibited conformation might bind actin strongly.

Global conformational changes from extended active states to folded inactive states have now been observed in several molecular motors. Vertebrate smooth and non-muscle myoII[17], kinesin[18] and myoV[8–10] all form folded conformations with higher sedimentation coefficients and decreased ATPase activity. Although the overall strategy used by various motors is similar, the details of the inactive state are tuned to the particular motor, its molecular architecture and its functional role in the cell.

The mechanism of ATPase inhibition differs for myoII and myoV despite the folded form of their inactive structures. In myoV, ATPase inhibition occurs for both heads by the same mechanism, namely binding of the cargo domain to loop 1, a feature known to affect rates of nucleotide exchange[16]. In contrast, a key feature of myoII inhibition was the striking asymmetry of the interaction between the two heads, indicating that ATPase activity of each head might be inhibited by a different mechanism[19]. The myoV lever arm is in a post-powerstroke orientation; the molecule is therefore likely to bind strongly to actin (see Fig. 4). In contrast, the lever arm of myoII is in a pre-powerstroke conformation, namely M–ADP–P_i (ref. 19), indicating that it should bind weakly to actin, in accord with results from biochemical studies[17]. The switch that activates myoV is the binding of calcium and/or cargo[9]. Activation by calcium was observed directly from ATPase measurements, whereas activation by cargo is inferred from the structure because cargo binding should compete with and disrupt the intramolecular interaction between the cargo and motor domains. Phosphorylation of the regulatory light chain is the switch that extends the folded conformation of smooth muscle myoII[17].

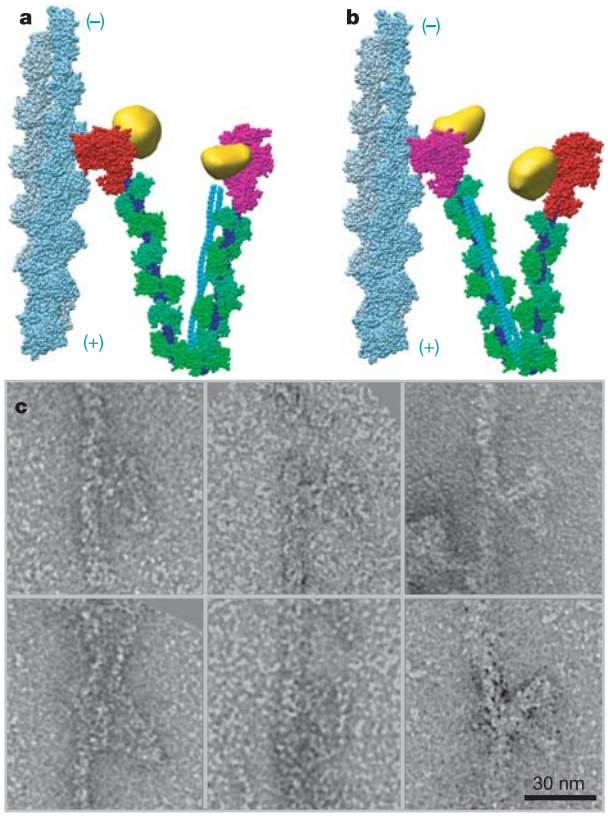

Figure 4 | Orientation of the myoV-inhibited structure on F-actin. F-actin strands rendered light blue and grey. Actin docking is based on ref. 30. **a**, Panel shows F-actin can bind only one myoV head at a time. The unbound head extends up towards the viewer. **b**, Same view direction as **a** but with the second head docked. **c**, High-magnification gallery of actin-bound myoV molecules. In some the S2 domain can be seen between the two heads. Drying in negative stain would flatten the structure onto a plane, which may account for some of the differences between the models and the micrographs.

The microtubule-based motor kinesin also undergoes a shift in sedimentation coefficient from about 6S to about 9S (refs 18, 20) that requires the cargo-binding domain. Artificial cargo can activate full-length kinesin, whereas shorter constructs are always active[21]. ATPase inhibition is due to slowed ADP release on the initial binding to microtubules, which keeps the microtubule-binding affinity weak[22].

The structures and properties of the inactive conformations of myoII and myoV indicate that there are likely to be unique mechanisms of motor recycling. MyoV is a barbed (+)-end-directed motor and once it delivers its cargo it has no obvious mechanism by which to return to its starting position to rebind cargo. Possible solutions would be simple diffusion or a set of recycling motors to carry the molecule back to its starting position. Both of these would require an inactive state with low affinity for actin, but our myoV structure indicates possible high actin-binding affinity.

An explanation may be found in the observation that, in brain, myoV co-localizes to regions such as growth cones[23] and dendritic spines[24], which have high rates of actin turnover indicative of active treadmilling[25]. We propose that actin treadmilling provides the recycling mechanism. MyoV cargo delivery would be akin to delivering a package by 'running up the down escalator'. Once the cargo has been delivered to the actin (+) end, myoV need only remain on the actin, which is facilitated by a conformation that inhibits ATP turnover but not actin binding. The treadmilling process on actin will eventually deliver the myoV to the actin filament (−) end, where new cargo binding can unfold and activate the molecule.

For this model to work, myoV must move at least twice as fast on actin as the actin filaments are growing. MyoV rates of movement on actin are of the order of 400 nm s^{-1} (refs 3, 15), whereas growth of the actin filament (+) end *in vivo* is about 10% of that by several measures[26]. Thus, myoV has the motor properties to 'run up the down escalator', and the binding properties to hang on for the return trip.

METHODS

Expression, purification and 2D crystallization. A Flag-tagged, full-length murine myoV was coexpressed with a calmodulin mutant deficient in Ca^{2+} binding (CaMΔall) in *Spodoptera frugiperda* (Sf9) cells, and purified as described previously[9]. Crystallization, similarly to previous efforts[19], used a buffer consisting of 20 mM Na_2HPO_4, 80–100 mM NaCl, 2 mM $MgCl_2$, 1 mM ADP, 1 mM EGTA and 8–9% poly(ethylene glycol) 8000. 1,2-dilauroyl-*sn*-glycero-3-phosphocholine was from Avanti Polar Lipids. Other reagents were from Sigma-Aldrich. The concentration of MyoV was 0.2 μM.

Electron microscopy and image processing. MyoV 2D arrays were recovered from the lipid monolayer on 200-mesh copper grids covered with a reticulated carbon film. We used correlation averaging and MSA to obtain averaged images of the coneflower motif and its six individual myoV molecules. Coneflower repeats were selected interactively by using the Boxer module of the EMAN software package[27]. Extracted coneflower repeats were corrected for contrast transfer function (phase-flipped) by using the EMAN CTFIT module. Averaging was performed by first aligning the individual coneflower repeats, followed by the extraction and alignment of the six individual molecules. Several cycles of MSA and multireference alignment were used to produce class averages.

Electron tomography. Specimens were frozen as described previously[19], transferred into a Gatan 626 cryoholder and examined under low-dose conditions in a Philips CM300-FEG electron microscope operated at 300 kV. Eight single-axis tilt series were collected at ×43,200 magnification with a Tietz F224HD 2,048-pixel × 2,048-pixel charge-coupled device camera and the associated EM-MENU software (TVIPS). The pixel size at the specimen level was 5.56 Å. Tilt series of about 60 images were collected from −70° to +70° with the use of cosine-rule increments. Three different defoci (−5, −8 and −12 μm) were used for data collection. The cumulative electron dose of each tilt series was about 30 electrons $Å^{-2}$.

Tilt-series images were aligned by using marker-free alignment[28]. For defocus determination, small patches at constant *y* coordinate and therefore at the same defocus were extracted and their power spectra were summed incoherently.

Defocus itself was determined with CTFIT[27]. Focus gradient correction[29] was applied to each image taken at more than 30° tilt, and a Wiener filter defocus correction was used for images with less than 30° tilt. The defocus-corrected images replaced the low-pass-filtered micrographs for further alignment refinement. Tomograms were computed by weighted back-projection.

3D average and correspondence analysis. Similarly to the 2D averaging, 3D averaging was performed in two steps. Coneflower repeats (200 pixels × 200 pixels × 80 pixels) were extracted from the cryotomograms, aligned in three dimensions and the six myoV molecules extracted (60 pixels × 80 pixels × 50 pixels). After all the myoV molecular volumes had been aligned to a single reference, they were classified with the use of hierarchical ascendant methods[11]. The 6,070 3D volumes were subjected to repeated cycles of multi-reference alignment and MSA until the signal-to-noise ratio no longer improved. In the final cycle, four class averages were generated; however, three of these, totalling 4,029 volumes, were judged to be very similar and were combined. The resolution of this average determined by Fourier Shell Correlation was 24 Å at the 0.5 cutoff. The 3D flower motif was generated by applying six-fold symmetry to the myoV molecule average.

Atomic model building. We constructed a myoV atomic model based on the high-resolution X-ray structure of the myoV–ADP motor domain plus the essential light chain structure (Protein Data Bank (PDB) accession number 1W7I)[13]. The rest of the lever arm was modelled on the X-ray structure of the calmodulin-like myosin light chain (Mlc1p) binding to the IQ2 and IQ3 motifs of yeast myosin Myo2p (PDB 1N2D)[12]. By repeating the IQ2 and IQ3 structures we built the IQ4, IQ5 and IQ6 complex. Because the 2D arrays were grown in ADP plus P_i, we tested the possibility that the lever arm was positioned in other orientations by rebuilding this structure at heavy-chain residue Ala 696 to conform to two other X-ray structures, PDB 1BR1 and 1QVI. These models were either poor fits to the density or produced structures that when docked on actin were flawed (Supplementary slideshow).

Received 15 January; accepted 15 March 2006.
Published online 16 April 2006.

1. Reck-Peterson, S. L., Provance, D. W. Jr, Mooseker, M. S. & Mercer, J. A. Class V myosins. *Biochim. Biophys. Acta* **1496,** 36–51 (2000).
2. Mehta, A. D. *et al.* Myosin-V is a processive actin-based motor. *Nature* **400,** 590–593 (1999).
3. Forkey, J. N., Quinlan, M. E., Shaw, M. A., Corrie, J. E. & Goldman, Y. E. Three-dimensional structural dynamics of myosin V by single-molecule fluorescence polarization. *Nature* **422,** 399–404 (2003).
4. Yildiz, A. *et al.* Myosin V walks hand-over-hand: single fluorophore imaging with 1.5-nm localization. *Science* **300,** 2061–2065 (2003).
5. Wang, F. *et al.* Effect of ADP and ionic strength on the kinetic and motile properties of recombinant mouse myosin V. *J. Biol. Chem.* **275,** 4329–4335 (2000).
6. Homma, K., Saito, J., Ikebe, R. & Ikebe, M. Ca^{2+}-dependent regulation of the motor activity of myosin V. *J. Biol. Chem.* **275,** 34766–34771 (2000).
7. Trybus, K. M., Krementsova, E. & Freyzon, Y. Kinetic characterization of a monomeric unconventional myosin V construct. *J. Biol. Chem.* **274,** 27448–27456 (1999).
8. Wang, F. *et al.* Regulated conformation of myosin V. *J. Biol. Chem.* **279,** 2333–2336 (2004).
9. Krementsov, D. N., Krementsova, E. B. & Trybus, K. M. Myosin V: Regulation by calcium, calmodulin, and the tail domain. *J. Cell Biol.* **164,** 877–886 (2004).
10. Li, X. D., Mabuchi, K., Ikebe, R. & Ikebe, M. Ca^{2+}-induced activation of ATPase activity of myosin Va is accompanied with a large conformational change. *Biochem. Biophys. Res. Commun.* **315,** 538–545 (2004).
11. Frank, J. *Three-Dimensional Electron Microscopy of Macromolecular Assemblies* (Academic, San Diego, CA, 1996).
12. Terrak, M., Wu, G., Stafford, W. F., Lu, R. C. & Dominguez, R. Two distinct myosin light chain structures are induced by specific variations within the bound IQ motifs-functional implications. *EMBO J.* **22,** 362–371 (2003).
13. Coureux, P. D., Sweeney, H. L. & Houdusse, A. Three myosin V structures delineate essential features of chemo-mechanical transduction. *EMBO J.* **23,** 4527–4537 (2004).
14. Tama, F., Miyashita, O. & Brooks, C. L. Normal mode based flexible fitting of high-resolution structure into low-resolution experimental data from cryo-EM. *J. Struct. Biol.* **147,** 315–326 (2004).
15. Cheney, R. E. *et al.* Brain myosin-V is a two-headed unconventional myosin with motor activity. *Cell* **75,** 13–23 (1993).
16. Sweeney, H. L. *et al.* Kinetic tuning of myosin via a flexible loop adjacent to the nucleotide binding pocket. *J. Biol. Chem.* **273,** 6262–6270 (1998).
17. Sellers, J. R. Regulation of cytoplasmic and smooth muscle myosin. *Curr. Opin. Cell Biol.* **3,** 98–104 (1991).
18. Hackney, D. D., Levitt, J. D. & Suhan, J. Kinesin undergoes a 9 S to 6 S conformational transition. *J. Biol. Chem.* **267,** 8696–8701 (1992).
19. Wendt, T., Taylor, D., Trybus, K. M. & Taylor, K. Three-dimensional image reconstruction of dephosphorylated smooth muscle heavy meromyosin reveals asymmetry in the interaction between myosin heads and placement of subfragment 2. *Proc. Natl Acad. Sci. USA* **98,** 4361–4366 (2001).
20. Stock, M. F. *et al.* Formation of the compact confomer of kinesin requires a COOH-terminal heavy chain domain and inhibits microtubule-stimulated ATPase activity. *J. Biol. Chem.* **274,** 14617–14623 (1999).
21. Coy, D. L., Hancock, W. O., Wagenbach, M. & Howard, J. Kinesin's tail domain is an inhibitory regulator of the motor domain. *Nature Cell Biol.* **1,** 288–292 (1999).
22. Hackney, D. D. & Stock, M. F. Kinesin's IAK tail domain inhibits initial microtubule-stimulated ADP release. *Nature Cell Biol.* **2,** 257–260 (2000).
23. Wang, F. S., Wolenski, J. S., Cheney, R. E., Mooseker, M. S. & Jay, D. G. Function of myosin-V in filopodial extension of neuronal growth cones. *Science* **273,** 660–663 (1996).
24. Espreafico, E. M. *et al.* Primary structure and cellular localization of chicken brain myosin-V (p190), an unconventional myosin with calmodulin light chains. *J. Cell Biol.* **119,** 1541–1557 (1992).
25. Star, E. N., Kwiatkowski, D. J. & Murthy, V. N. Rapid turnover of actin in dendritic spines and its regulation by activity. *Nature Neurosci.* **5,** 239–246 (2002).
26. Forscher, P. & Smith, S. J. Actions of cytochalasins on the organization of actin filaments and microtubules in a neuronal growth cone. *J. Cell Biol.* **107,** 1505–1516 (1988).
27. Ludtke, S. J., Baldwin, P. R. & Chiu, W. EMAN: semiautomated software for high-resolution single-particle reconstructions. *J. Struct. Biol.* **128,** 82–97 (1999).
28. Winkler, H. & Taylor, K. A. Accurate marker-free alignment with simultaneous geometry determination and reconstruction of tilt series in electron tomography. *Ultramicroscopy* **106,** 240–254 (2006).
29. Winkler, H. & Taylor, K. A. Focus gradient correction applied to tilt series image data used in electron tomography. *J. Struct. Biol.* **143,** 24–32 (2003).
30. Rayment, I. *et al.* Structure of the actin–myosin complex and its implications for muscle contraction. *Science* **261,** 58–65 (1993).

Supplementary Information is linked to the online version of the paper at www.nature.com/nature.

Acknowledgements We thank H. Winkler for his guidance in focus gradient correction and 3D volume classification. We also thank the National Institutes of Health Research Resource for MMTSB and C. L. Brooks 3rd for making NMFF available. This research was supported by grants from the National Institutes of Health (to K.M.T. and K.A.T.).

Author Information The atomic coordinates of the final myoV atomic model have been deposited in the Protein Data Bank with accession number 2DFS. The density volume for the flower motif shown in Fig. 2 has been deposited in the European Bioinformatics Institute under accession code EMD-1201. Reprints and permissions information is available at npg.nature.com/reprintsandpermissions. The authors declare no competing financial interests. Correspondence and requests for materials should be addressed to K.A.T. (taylor@bio.fsu.edu) or K.M.T. (trybus@physiology.med.uvm.edu).